

REPORT DOCUMENTATION PAGE				<i>Form Approved</i> OMB No. 0704-0188	
<small>Public reporting burden for this collection of information is estimated to average 1 hour per response, including the time for reviewing instructions, searching existing data sources, gathering and maintaining the data needed, and completing and reviewing this collection of information. Send comments regarding this burden estimate or any other aspect of this collection of information, including suggestions for reducing this burden to Department of Defense, Washington Headquarters Services, Directorate for Information Operations and Reports (0704-0188), 1215 Jefferson Davis Highway, Suite 1204, Arlington, VA 22202-4302. Respondents should be aware that notwithstanding any other provision of law, no person shall be subject to any penalty for failing to comply with a collection of information if it does not display a currently valid OMB control number. PLEASE DO NOT RETURN YOUR FORM TO THE ABOVE ADDRESS.</small>					
1. REPORT DATE (DD-MM-YYYY)		2. REPORT TYPE		3. DATES COVERED (From - To)	
4. TITLE AND SUBTITLE				5a. CONTRACT NUMBER	
				5b. GRANT NUMBER	
				5c. PROGRAM ELEMENT NUMBER	
6. AUTHOR(S)				5d. PROJECT NUMBER	
				5e. TASK NUMBER	
				5f. WORK UNIT NUMBER	
7. PERFORMING ORGANIZATION NAME(S) AND ADDRESS(ES)				8. PERFORMING ORGANIZATION REPORT NUMBER	
9. SPONSORING / MONITORING AGENCY NAME(S) AND ADDRESS(ES)				10. SPONSOR/MONITOR'S ACRONYM(S)	
				11. SPONSOR/MONITOR'S REPORT NUMBER(S)	
12. DISTRIBUTION / AVAILABILITY STATEMENT					
13. SUPPLEMENTARY NOTES					
14. ABSTRACT					
15. SUBJECT TERMS					
16. SECURITY CLASSIFICATION OF:			17. LIMITATION OF ABSTRACT	18. NUMBER OF PAGES	19a. NAME OF RESPONSIBLE PERSON
a. REPORT	b. ABSTRACT	c. THIS PAGE			19b. TELEPHONE NUMBER (include area code)

Final Report

Research and Development of a High Power Laser Driven Electron Accelerator Suitable for Applications

Donald Umstadter, P.I.
Sudeep Banerjee
Bradley Shadwick

Grant/Contract Number: FA9550-09-1-0009

June 12, 2011

Contents

A	Executive Summary	2
B	Personnel Involved in Research Effort	3
C	Introduction	4
D	Phase II Task Summary	4
	D.1 Module I: High-Energy Electron Accelerator	4
	D.2 Module II: High-Energy Ion Accelerator	5
	D.3 Theory and Numerical Simulations in Support of Ac- celerator Experiments	5
	D.4 Application of Electron and Ion Beams to Radiography	5
E	Detailed Report by Task	5
	E.1 Automation and feedback control of laser and accelerator	5
	E.2 Increase energy of accelerator from 0.4 GeV to >1 GeV, and increase beam charge	9
	E.3 Control of energy spread and tunability of accelerator .	12
	E.4 Generation of ion beams with PW laser pulses	16
	E.5 PIC and fluid simulations of electron and ion acceleration	22
	E.6 Study limits of resolution and target thickness for imag- ing embedded cracks in DoD relevant samples with both electrons and ions beams	25
F	Progress towards program goals	31
G	Publications	32
	G.1 Refereed journals	32
	G.2 Conference proceedings	32
	References	33

A Executive Summary

During Phase I of the HRS program, the team from the University of Nebraska, Lincoln (UNL) made use of the unique capabilities of their high-power laser system to perform an extensive study of the physical phenomena and control mechanisms involved in one such module: the conversion of laser light into high-brightness, nearly monoenergetic electron beams. During Phase II of the project, we continued work on the development of laser-driven accelerators. The work performed encompassed the generation and optimization of tunable, high-energy electron beams from underdense plasma, stabilization of the laser system to enable reliable operation of the accelerator, as well as detailed numerical, and theoretical work to predict and improve the performance of the electron accelerator. Stable electron beams in the energy range 100 – 500 MeV were demonstrated, and it was shown that the energy could be tuned in a straightforward way by changing laser and plasma parameters, without loss of beam quality. These beams had low angular divergence (1 – 4 mrad), and small energy spread ($\sim 5 - 25\%$), with a resulting brightness $\sim 10^{11}$ electrons mm^{-2} MeV^{-1} mrad^{-2} . The high-energy electron beams produced were used for radiographic applications. High resolution (sub-mm) studies of voids embedded in 2-in thick stainless steel blocks were successfully performed. Electron-beam energies of 600 – 800 MeV were attained by the use of longer interaction length (5 – 10 mm jets) and higher laser power (80 – 100 TW). Detailed particle-in-cell simulations have been performed to elucidate the mechanism underlying the generation of these high-brightness electron beams. These studies, in conjunction with analytical models, explain the role of focusing geometry in suppressing continuous injection, which results in dark-current-free beams. The stability and performance of the laser system has been improved by incorporating multiple diagnostics and active beam stabilization of the amplifier stages. Real-time diagnostics of the beam characteristics on target have also been implemented in order to precisely correlate the electron beam characteristics with measured experimental parameters. The laser system has been upgraded to PW peak power by the addition of a new amplifier and compressor, and will enable studies on the generation of energetic proton beams.

B Personnel Involved in Research Effort

Donald P. Umstadter, Principal Investigator
Bradley A. Shadwick, Assistant Professor
Vidya Ramanathan, Post-Doctoral Research Assoc.
Sudeep Banerjee, Research Assistant Professor
Chakra M. Maharjan, Post-Doctoral Research Assoc.
Alok Srivastava, Post-Doctoral Research Assoc.
Nathaniel Cunningham, Post-Doctoral Research Assoc.
Isaac Ghebregziabher, Post-Doctoral Research Assoc.
Suman Bagchi, Post-Doctoral Research Assoc.
Jun Zhang, Post-Doctoral Research Assoc.
Kun Zhao, Post-Doctoral Research Assoc.
Shouyuan Chen, Post-Doctoral Research Assoc.
Scott Sepke, Post-Doctoral Research Assoc.
Anand Moorti, Post-Doctoral Research Assoc.
Nathan Powers, Graduate Student
Matthew Rever, Graduate Student
Nate Chandler-Smith, Laser Optical Engineer
Kevin Brown, Laser Optical Engineer
James Kayser, Laser Optical Engineer
Serguei Kalmykov, Senior Research Assoc.
Ashley Ernesti, Undergraduate Student
Laila Gharzai, Undergraduate Student
Frank Lee, Undergraduate Student
Jeffrey Thomas, Undergraduate Student
Melissa Zephier, Undergraduate Student
Bertram Gay, Undergraduate Student
Barb Rebrovich, Grants Co-ordinator
Sara Mattson, Grants Co-ordinator

C Introduction

During Phase I of the Hyperspectral Radiography Sources (HRS) program, the team from the University of Nebraska, Lincoln (UNL) made use of the unique capabilities of their high-power laser system to perform an extensive study of the physical phenomena and control mechanisms involved in Module 1: the conversion of laser light into high-brightness, nearly monoenergetic electron beams. Using 40 – 50 TW of peak laser power to drive a self-guided laser wakefield, they demonstrated record-setting electron beam characteristics: an energy of 320 ± 28 MeV, an angular divergence of 5 mrad, and a charge of 1 – 100 pC. Remarkably, the acceleration region was only 3-mm in length. The use of a stable and well-characterized laser system, in conjunction with high-contrast, and adaptive optical correction, resulted in highly reproducible electron beams, both in terms of energy and pointing stability. Operation in the resonant regime, where the spatial and temporal dimensions of the laser pulse equals the plasma wavelength and period, respectively, was also found to dramatically improve beam brightness and reproducibility.

D Phase II Task Summary

D.1 Module I: High-Energy Electron Accelerator

Task 1: Automation and feedback control of laser and accelerator

Milestone: Feedback-stabilized laser system and accelerator

Task 2: Increase energy of accelerator from 0.4 GeV to > 1 GeV, and increase beam charge

Milestone: Near GeV electron beam with charge of 0.1 – 0.5 nC per shot

Task 3: Control of energy spread and tunability of accelerator

Milestone: Controllable electron beams with respect to beam energy and energy spread

D.2 Module II: High-Energy Ion Accelerator

Task 4: Generation of energetic ion beams from underdense plasma

Milestone: 1 – 10 MeV ion beams from underdense media

Task 5: Generation of ion beams with PW laser pulses

Milestone: 10 – 100 MeV ion beams from underdense media

D.3 Theory and Numerical Simulations in Support of Accelerator Experiments

Task 6: PIC and fluid simulations of electron and ion acceleration

Milestone: Fluid and PIC simulations to predict performance of Modules 1 and 2 and benchmarking of theoretical results against experimental observations

D.4 Application of Electron and Ion Beams to Radiography

Task 7: Study limits of resolution and target thickness for imaging embedded cracks in DoD relevant samples with both electrons and ions beams

Milestone: Imaging of cracks in structures of interest to DoD

E Detailed Report by Task

E.1 Automation and feedback control of laser and accelerator

In order to have stable, and reliable performance of laser-driven accelerators, it is critical to ensure that the laser performance is optimal and stable. Several diagnostic and control subsystems are required: extensive diagnostics to monitor the many stages of the laser system, active and passive control of the system performance, precise measurement of the laser pulse characteristics on target, and feedback control of pulse characteristics to optimize accelerator performance. During phases I and II of the project, we have successfully implemented numerous modules to characterize, and control the performance of the laser chain, including real-time diagnostics of the pulse parameters on target. A brief summary of these is provided below.

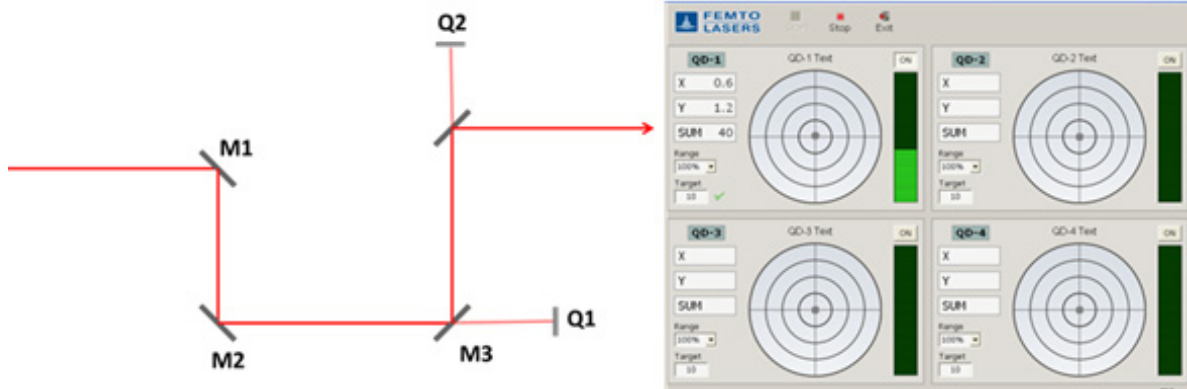


Figure 1: Pointing stabilization of laser using two motorized mirrors and two quad cells. Principle of the system is shown on the left panel (explained in text) and display of the system in operation is shown on the right panel. The system operates in a feedback loop to preserve the axis of the beam from one stage of the laser to the next. A simplified version based on one motorized mirror and one quad cell is also used in location where angular drift is the dominant contribution to degradation of beam pointing.

Beam pointing stabilization with active feedback

In the early stages of the laser system, the beam diameter is small (few mm) resulting in significant beam pointing, and drift instabilities. In order to minimize the drift of the beam from one stage to the next we have implemented an active stabilization unit [1, 2] to control the pointing of the beam from the oscillator into the stretcher, from the stretcher into the first multi-pass amplifier, as well between the first multi-pass amplifier to the pre-amplifier. The principle of the system is shown in Fig. 1 (left-panel). Two motorized mirrors ($M1$ and $M2$) and two quad cell ($Q1$ and $Q2$) are used to maintain the axis of propagation of the beam. Mirror $M1$ corrects for deviation of beam centroid on quad $Q1$ and maintains beam position on mirror $M3$. Mirror $M2$ works in conjunction with quad $Q2$, and preserves the angle of the beam after reflection from mirror $M3$. With the two correction stages operating in tandem, the beam axis after reflection from mirror $M3$ is preserved. The system displays the beam centroid as shown in Fig. 1 (right panel). Since angular drift is often the dominant contribution to loss of beam pointing, we have also implemented a simplified version of the system, that uses the equivalent of mirror $M2$ and quad $Q2$ to correct for angular deviations.

Real-time monitoring of amplified beam profile

Since the beam is amplified to extremely high-energy, it is important to ensure that the beam as it propagates through the various amplification stages is uniform. This is critical at specific planes - in particular when the beam is incident on the crystal face in the large power amplifiers. Two modules were implemented to image the beam on the crystal faces, that amplifies the pulse from 50 mJ to 2 J, and from 2 J to 5 J. The layout of the system is shown in Fig. 2 (left-panel). A high-dynamic range CCD is used to ensure precise measurement of the beam profile. The system is controlled by custom software that was developed in our laboratory. The software provides for real time display of the beam profile, line-outs along two orthogonal axes and the capability to store the recorded images at a fixed frame rate. Real-time monitoring of the laser system is critical to ensure that a high-quality beam is amplified at all times. Spatial non-uniformity in the beam can increase the local flux on optical components leading to damage of critical parts.

Besides monitoring of the beam profile at these critical stages, periodic checks are performed on subsystems such as the pump laser to ensure that the beam quality is optimal for pumping and seeding the power amplifiers. A number of safety and operational interlocks have been implemented in the system. A hardware controlled spectral interlock, prevents seeding of the amplifier unless the spectral bandwidth of the IR pulse is above a user-specified limit. The laser chain is also protected from backscattered radiation seeding the amplifier. A critical aspect of the system is the ability to precisely compress the stretched and amplified pulse, since optimal accelerator operation is obtained for the shortest laser pulse. Central to this is the parallelism of the gratings in the pulse compressor. If the gratings are not parallel to each other, a spatial chirp will be introduced in the laser beam, as a result of which different wavelengths are focused on different spatial locations. This degrades the quality of the laser focus quality and reduces the laser intensity on the gas target. Since the grating parallelism can be affected by the mechanical drift of the grating mount and vibration from background, it is critical to monitor this parameter in real time to eliminate the spatial chirp in the laser beam. The grating parallelism can be checked by examining the overlap of the different diffraction orders from the reflection of a helium neon laser beam [3]. By observing the interference pattern of the overlapped beams, the

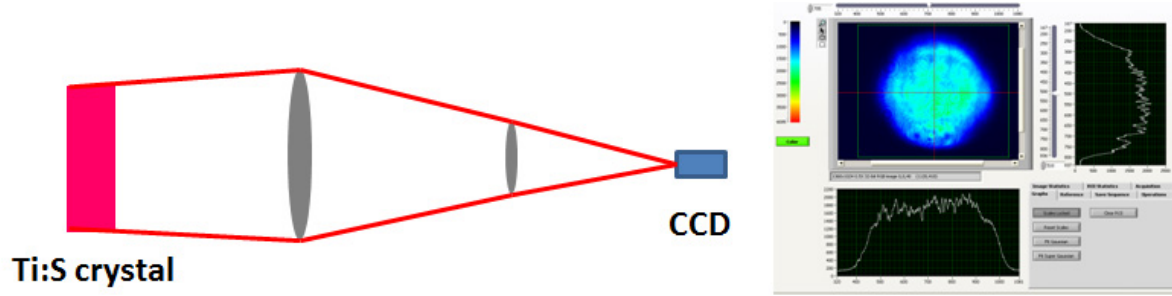


Figure 2: Spatial uniformity of amplified beam is monitored by imaging the face of the Ti:S crystal to a CCD using a set of lenses. The optical system used to demagnify and image the beam is shown on the left panel. The panel on the right shows a typical beam profile and lineouts along the central axis. A nearly flat-top profile, with small modulations, corresponds to good alignment for the laser chain.

grating parallelism can be monitored in real time and corrected by rotating the gratings. This measurement guarantees a chirp-free compressed pulse.

Real-time measurement of pulse parameters on target

For efficient operation of the accelerator and to draw correlations between experimental data and laser and plasma conditions, it is critical to know the pulse characteristics for every shot fired on target. Despite, diligent effort, the beam characteristics drift with time and there exist small-scale fluctuations in both space, and time. An extensive diagnostic system has been implemented in order to precisely measure all characteristics of the laser pulse on target. The system is shown in Fig. 3. A small fraction of the beam delivered on target is sampled using a beamsplitter that reflects 99% of the incident pulse and transmits 1%. The transmitted pulse is transported to the diagnostic setup, down-collimated, and split into several components. The pulse energy is measured with a calibrated photo-diode, and the nanosecond contrast by a fast photodiode with a rise-time of 1 ns. The diagnostic setup shown in Fig. 3 measures the pulse characteristics in spatial, spectral, and time domain. In the spatial domain, the wavefront of the pulse is measured by the SID-4 wavefront sensor which uses shearing interferometry. The wavefront sensor is connected to a deformable mirror in a feedback loop and corrects the spatial aberrations of the beam [4]. The Strehl ratio after correction is >0.9 corresponding to a nearly diffraction limited focal spot on target. The beam is focused by a 1 m focal length lens onto a CCD and provides an

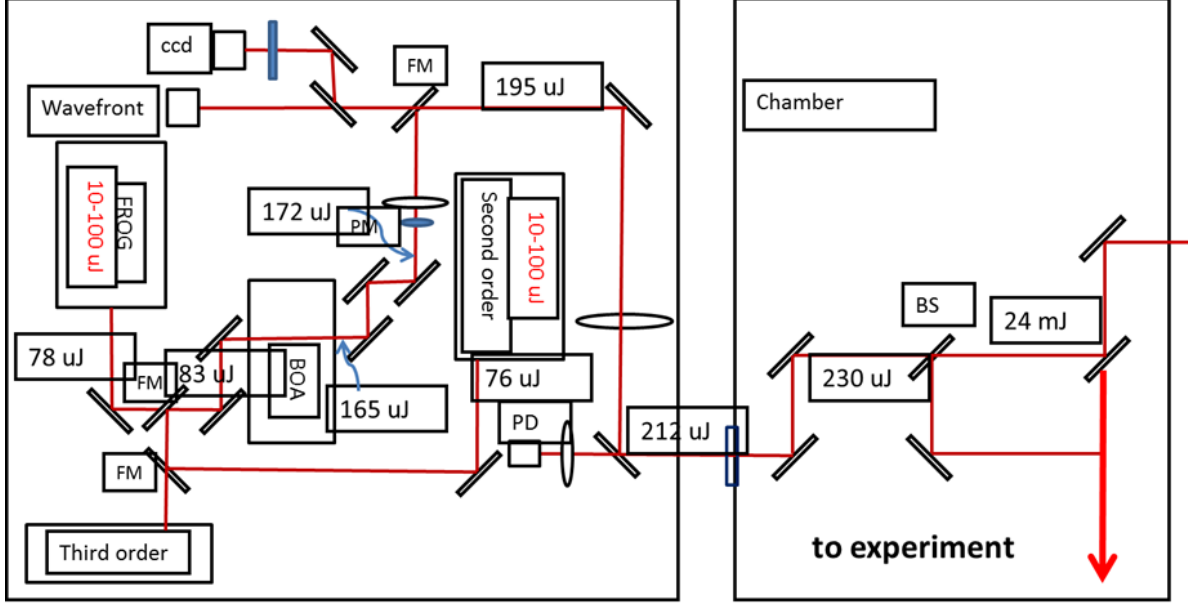


Figure 3: Setup for characterization of laser pulse on target. A leakage beam is transported to the diagnostic set-up and the pulse characterized spatially, spectrally, and temporally. A subset of the measurements can be recorded in real-time and correlated with experimental data.

equivalent plane image of the focal spot on target and this can be monitored in real time. A fiber coupled spectrometer is used to measure the spectrum of the pulse: this is needed since spectral loss will result in temporally long pulses. The temporal duration of the pulse as well as spatial chirp are characterized in detail by measurement of the temporal amplitude and phase. This is done using the technique of frequency resolved optical gating (FROG) [5]. Picosecond temporal pulse characteristics are measured using a third-order cross-correlator. Energy, nanosecond contrast and equivalent plane focusing are measured in real-time. A forward imaging set-up is also in place to measure the characteristics of the transmitted pulse after it propagates through the plasma. This is used to measure the absorption of the pulse in the medium, image the focal spot on target as well as correlate spectral changes with the generation of monoenergetic electron beams.

E.2 Increase energy of accelerator from 0.4 GeV to >1 GeV, and increase beam charge

Previously, we reported on the generation of 100 – 400 MeV electron beams, using 40 – 70 TW laser pulses. Higher energy electron beams are produced

by using longer acceleration lengths and high laser power. The experiments were carried out with the 100 TW laser DIOCLES [33]. The system produces linearly polarized pulses with a central wavelength $\lambda_0 = 0.805 \mu\text{m}$, maximum energy 3.5-J at 10-Hz repetition rate, and pulse duration $\tau_L = 30 \text{ fs}$ (FWHM). The laser beam is incident on a deformable mirror that operates in a feedback loop with a wavefront sensor. The 70-mm diameter laser pulse with spatial aberrations corrected, is focused to a nearly diffraction limited spot (Strehl ratio ~ 0.95) using a one meter focal length dielectric-coated off-axis paraboloid. The intensity profile in the central spot (shown in the inset of Fig. 4) allows a Gaussian fit with a radius $r_0 = 13.6 \mu\text{m}$; 70% of incident energy is contained within a diameter $2r_0$. High-energy beams were generated using 80 – 100 TW laser power on target. The laser pulse was spatially and temporally characterized at full power using a multi-stage beam sampling system. The energy on target was varied using a combination of a waveplate and polarizers. The temporal duration is optimized by varying the separation between the compressor gratings, and adjusting the second and third order phase by use of a spectral phase modulator. The shot-to-shot pointing stability of the laser pulse on target was $\pm 7 \mu\text{rad}$.

The experimental setup is presented in Fig. 4. The target is a high-density jet of neutral helium produced by a 5, 7.5, and 10 mm diameter supersonic slit nozzles (modified Laval type). The neutral density profile (characterized interferometrically) has symmetric downramps along the edges extending over 0.5 mm, with a flat-top central region. The laser pulse is focused before the front edge of the nozzle. During the experiments, an equivalent plane imaging system locates the longitudinal position of focal plane with a precision $\pm 0.5 \text{ mm}$. The focused pulse fully ionizes the medium producing a plasma with $n_{e0} = (0.4 - 5) \times 10^{19} \text{ cm}^{-3}$. At $n_{e0} < 2 \times 10^{19} \text{ cm}^{-3}$, images of the plasma emission at 800 nm show a uniform laser-created plasma column spanning the entire jet length. The accelerated electrons exiting the plasma impinge on a fluorescent screen (LANEX) that is imaged with a 12-bit CCD. The absolute response of LANEX to electrons, calibrated using an 18 MeV radio-frequency linear accelerator (Siemens Primus), is used to obtain the charge in a specified energy interval. Electron energy is measured using a magnetic spectrometer operating in a slit-free geometry and having a range of 20 – 800 MeV. The energy resolution is better than 10% at 500 MeV, and rapidly degrades beyond 800 MeV. The spectrometer response function

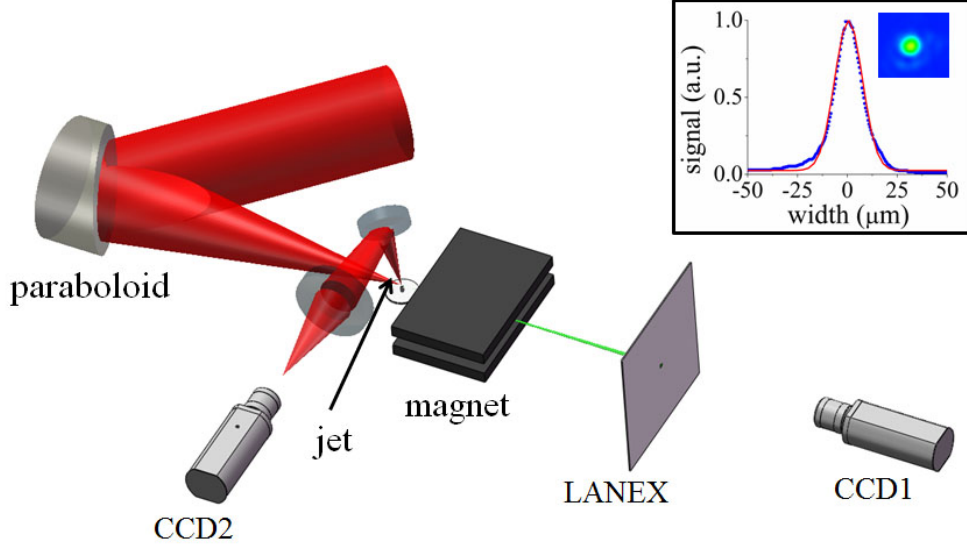


Figure 4: Schematic of the experimental setup. The high-power laser pulse is focused at the front edge of a supersonic helium gas jet. The pulse propagation is monitored by imaging the Thomson scattered light using CCD2. Electrons passing through a magnetic spectrometer impinge on a LANEX screen. Optical emission from the LANEX is imaged onto the CCD1 to measure the electron beam angular divergence and energy spectrum. Inset: image of the laser focal spot in vacuum (full-power shot) and its vertical and horizontal lineouts.

has been modeled with the General Particle Tracer (GPT) code [34], and the final energy distribution is obtained, taking into account the finite beam divergence.

In order to generate >500 MeV energy electron beams, the high-power laser pulse (70–90 TW) is focused onto a 5 mm supersonic jet. The laser pulse self-channels through the medium and stays focused over the entire 5 mm of the jet. The specific experimental geometry and associated measurements is shown in Fig. 5. The channeling of the laser pulse through the jet is imaged and the result is shown in Fig. 5(b). The laser stays self-focused over the entire 5 mm length of the jet. Experiments with longer jets show similar results and a self-focused distance of 10 mm has been observed. This corresponds to propagation over nine Rayleigh ranges. Under these conditions high-energy electron beams are observed. The spatial profile of the electron beam is shown in Fig. 5(c). The angular profile shows an electron beam with a divergence of 1.5 mrad.

A detailed study was performed to study the characteristics of the electron beam produced from longer acceleration length slit nozzles. The laser and

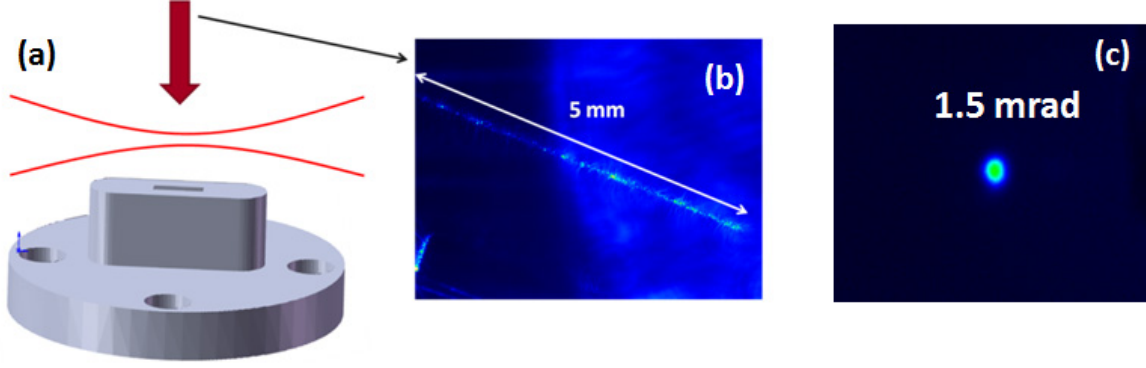


Figure 5: Generation of high-energy electron beams with 5 mm supersonic nozzles. The high-power laser pulse is focused onto the supersonic nozzle (a) and self-channels through the entire length of the nozzle as shown in (b). The low-divergence electron beam produced is shown in (c).

plasma parameters were varied in as described in prior reports. A trend similar to that observed with shorter acceleration length results - at high densities, the electron beams have lower energy and are unstable with respect to angle and energy. Optimum beams are obtained for plasma density of $8 \times 10^{18} \text{ cm}^{-3}$. A sequence of electron beams is shown in Fig. 6. For these conditions, monoenergetic beams with peak energy $> 700 \text{ MeV}$ are observed. The beams have a pointing stability $\sim 5 \text{ mrad}$. The energy spread is larger than observed with the 3 – 4 mm nozzle. We are in the process of optimizing the electron beam characteristics with these longer interaction length nozzles.

E.3 Control of energy spread and tunability of accelerator

A detailed parametric study was used to control the energy spread of the electron beams and tune the electron energy over a broad range. The experimental setup is the same as described in the previous section. The target is a high-density jet of neutral helium produced by a 3 or 4 mm diameter supersonic Laval nozzle. The neutral density profile (characterized interferometrically) has symmetric downramps along the edges extending over 0.5 mm, and a 2 or 3 mm central flat region. The laser pulse is focused before the front edge of the nozzle. Electron energy is measured using a magnetic spectrometer operating in a slit-free geometry and having a range of 20 – 500 MeV. The energy resolution is better than 10% at 300 MeV, and rapidly degrades beyond 400 MeV. With the laser power and the target length fixed,

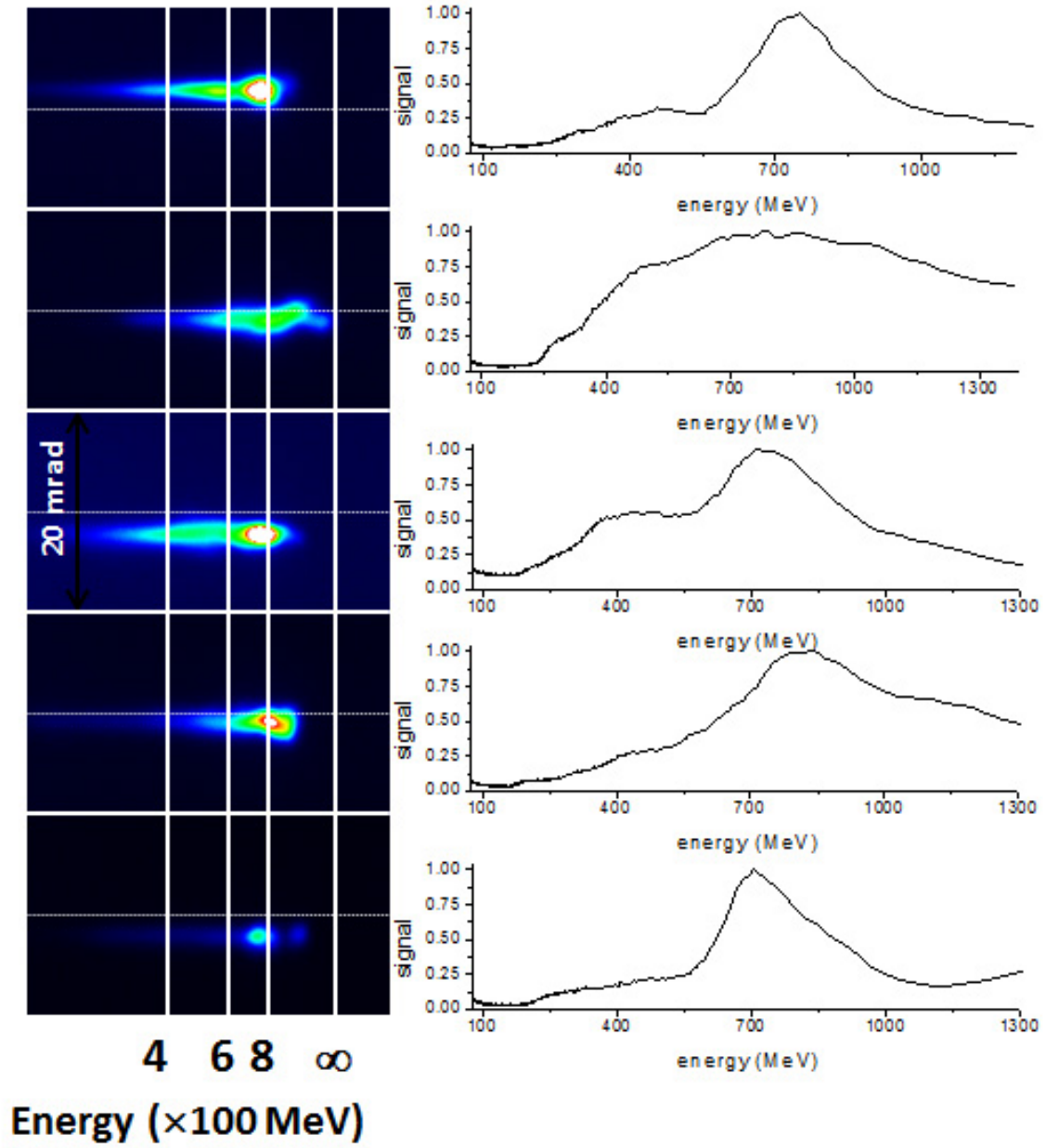


Figure 6: Spectrally dispersed high-energy electron beams produced from the interaction of 80 TW laser pulses with a 5 mm slit nozzle. The solid vertical lines provides guides for the energy spectrum. Horizontal dotted lines correspond to the mean angular position. The beam charge ranges from 10 – 100 pC.

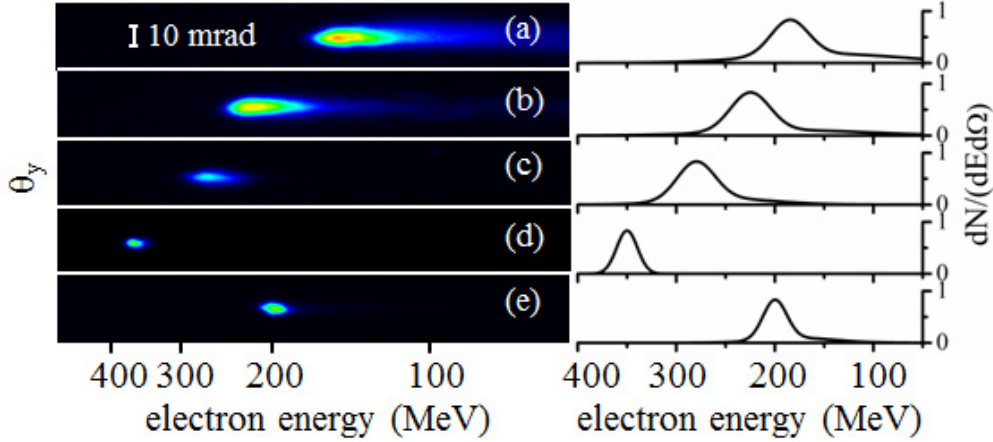


Figure 7: Spectrally dispersed electron beams at the exit of magnetic spectrometer and corresponding lineouts of electron spectra deconvolved using the GPT code taking into account the spectrometer response function and electron beam divergence. Statistics and brightness for these beams are shown in Table 1. Panels (a) – (e) correspond to plasma densities 12 ; 9 ; 7.2 ; 6 ; and $4.8 \times 10^{18} \text{ cm}^{-3}$, respectively. The jet length is 3 mm. The laser power on target is 42 TW.

the plasma density was scanned by varying the backing pressure on the nozzle until electron beams of the highest quality were produced.

The position of the laser focal plane with respect to the nozzle was kept constant over the entire series of shots. The evolution of single-shot energy spectra is presented in Fig. 7; multi-shot electron beam statistics for each set of parameters are summarized in Table 1. The dark current component of the beam is quantified by computing the *contrast*, defined as the ratio of the charge within the FWHM of the quasi-monoenergetic peak to the total charge on the LANEX. If significant dark current is present, the contrast would be low, and vice versa. As demonstrated by the data of column C of Table 1, the optimal beams have the highest contrast, ~ 0.75 (same as for an ideal Gaussian distribution). Hence, all the charge is contained in the monoenergetic peak, with no detectable charge at other energies – the beam is dark-current-free. The presence of a low-energy tail noticeably reduces the contrast; at higher densities, when the beam becomes polychromatic, the contrast is the lowest.

This near-threshold operating regime is scalable: an optimal density can be found for different laser powers, and acceleration lengths, leading to a stable, dark-current-free, quasi-monoenergetic electron beam [similar to that

	E	$\Delta E/E$	D	P	Q	B	C
(a)	185	0.24	4.3	± 3	240	19	0.46
(b)	225	0.21	3.9	± 2.8	85	7.5	0.55
(c)	280	0.16	2.7	± 1.8	27	5.5	0.64
(d)	350	0.07	2.3	± 1.1	7	8.5	0.75
(e)	200	0.12	3.1	± 1.7	20	4.4	0.62

Table 1: Electron beam characteristics for the parameters of Fig. 2 averaged over 10 – 30 shots; E is the central energy in MeV; $\Delta E/E$ is the normalized energy spread (FWHM); D is the FWHM divergence in mrad; P is the pointing stability in mrad; Q is the charge in pC; B is the brightness (per shot) in units of 10^{10} electrons $\text{MeV}^{-1} \text{mm}^{-2} \text{mrad}^{-2}$; and C is the ratio of the charge within FWHM in energy to the total beam charge. The measured beam charge fluctuation is 50%.

shown in Fig. 7(d)]. Example of such optimal beams obtained over a broad range of laser, and plasma parameters are shown in Fig. 8.

The pointing stability of electron beams is found to be sensitive to the pulse contrast [35]. Reduction of shot-to-shot pointing variation to a few milliradians requires nanosecond contrast of 2×10^{-8} , which is achieved by optimizing the timing of the Pockels cells in the laser chain, and the time delay between the pump, and seed beams in all amplification stages. Table 1 shows that the pointing angle fluctuation is below the beam divergence in the entire range of densities $(4.8 - 12) \times 10^{18} \text{cm}^{-3}$, which is opposite to the observations made in earlier experiments with high density plasmas [27, 28, 29]. At the optimal operation point, $n_{e0} = 6 \times 10^{18} \text{cm}^{-3}$, the measured pointing fluctuation reaches the minimum, ± 1.1 mrad.

The results of Fig. 7 imply that a self-injection threshold corresponds to the laser power ten times higher than the critical power for relativistic self-focusing. In all cases presented in Fig. 7, and Fig. 8, beam loading is too weak to suppress self-injection [36]. Thus, the only way to terminate injection is to limit the plasma length. Reducing the plasma density slows focusing of the pulse, delaying formation of the bubble. Below the cutoff density [e.g. the case of Fig. 7(e)], the bubble does not form during the laser transit through the plasma, and self-injection into the first bucket does not occur. At the optimal density [e.g. the case of Fig. 7(d)], the bubble forms before the end of the plasma, experiences minimal evolution, and creates a quasi-monoenergetic electron bunch [19, 21]. The plasma ends before either the laser waist oscillates [20] or pulse self-compresses [37, 21]; hence, injection into the bubble does not resume, and the continuous low-energy tail does not

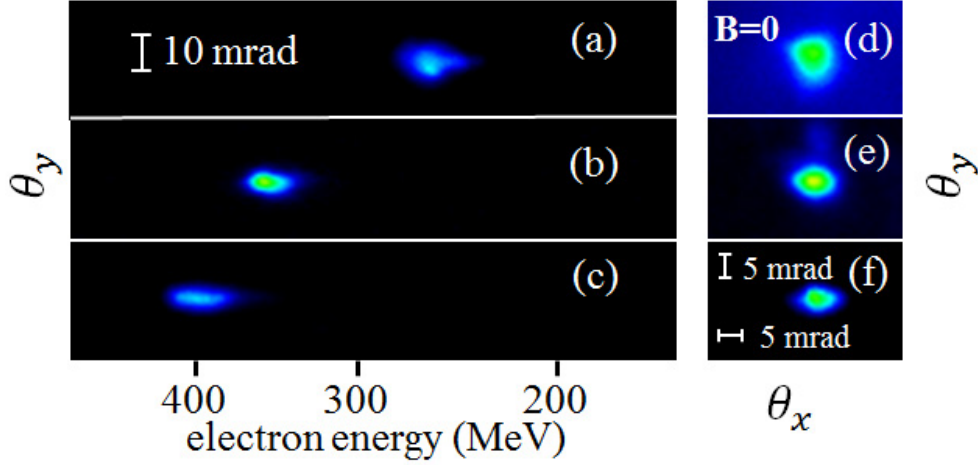


Figure 8: Images of spectrally dispersed (left) and undeflected (right) background-free electron beams as a function of laser power and plasma density: (a,d) $P = 34$ TW, $n_{e0} = 7.8 \times 10^{18} \text{ cm}^{-3}$; (b,e) $P = 42$ TW, $n_{e0} = 6 \times 10^{18} \text{ cm}^{-3}$; (c,f) $P = 58$ TW, $n_{e0} = 5.3 \times 10^{18} \text{ cm}^{-3}$. Halo in panel (b) is produced by low-energy background (< 10 MeV) present at high-densities, which is not seen after the magnet. Images (a) and (c) are obtained with a 3 mm jet. Image (e) is obtained with a 4 mm jet and a higher-resolution spectrometer. θ_x and θ_y denote the divergence angle in the horizontal and vertical direction.

form.

We confirm this interpretation with three-dimensional particle-in-cell (3D PIC) simulations using pre-ionized helium plasma with a trapezoidal profile (0.5 mm linear entrance, and exit ramps and a 2 mm plateau) and a Gaussian laser pulse with 42 TW power, central wavelength $0.805 \mu\text{m}$, duration 30 fs, and waist $13.6 \mu\text{m}$. In all simulations, the plasma extends from $z = 0$ to 3 mm. The simulated beam characteristics are found to be in good agreement with experimental observations, and confirm the postulated mechanism describe above. Further results on simulation of the acceleration process are described later in the report.

E.4 Generation of ion beams with PW laser pulses

The PW system at UNL is a unique high-power laser system. The pump lasers for the PW amplifier have not met the specifications during factory tests: the beam profile at 1m from the exit if the laser is modulated. This prevented the pumping of the large Ti:S crystal. Since this is a custom built pump laser, the manufacturer was not able to anticipate that this problem

would arise. The issue has been corrected by the use of 4 additional phase plates to be installed by the manufacturer. However there was a significant time delay in procurement of the phase plates. It was critical that these phase plates have been installed and the performance of the laser verified prior final use. The satisfactory performance of the pump lasers significantly delayed the project. As a result of the challenges associated with the PW system, only preliminary work was performed on the development of a laser driven ion accelerator.

In order to enable the development of a laser-driven ion accelerator, the 100 TW laser system was upgraded to the PW level. The central feature of the proposed laser upgrade project was the development of a petawatt high-energy laser amplifier, by the addition of a multi-pass amplifier and a pulse compression system for the amplified laser pulse. The layout of the complete laser system is shown in Fig. 9. The original system comprised of an oscillator, stretcher, and multi-pass amplifiers produced 5-J per pulse at 10-Hz repetition rate. The amplified pulse was compressed to 30-fs pulse duration in a standard two-grating pulse compressor and resulted in a peak power of > 100 TW. The laser system has been upgraded to the 1-PW peak power level with an additional power amplifier and pulse compressor. The upgrade to the system consists of the following: (a) high-energy pump lasers, (b) power amplifier, (c) pulse compressor, and (d) diagnostics. The specifics of each are provided in detail below. Once amplified and compressed, the light is transported to the target chamber and alignment assembly by means of the beam transport optical assembly. Characterization of the beam takes place in the diagnostic assembly, which is composed of photodiodes, ccd cameras, control computers, energy meters, spectrometer, FROG and third-order cross-correlator.

Pump lasers: The pump lasers are based on Nd-glass technology and are designed to produce ~ 25 J of energy per pulse at 527 nm at a repetition rate of 0.1 Hz. The layout and specifications are shown in Fig. 10. The lasers were designed and built to meet stringent specifications in order to ensure that the pump beam profile is of acceptable quality to pump a Ti:S amplifier. The pump lasers were shown to meet all the specifications excepting for spatial homogeneity of the output beam profile. The manufacturer of the system provided (at no-cost) a phase plate at the exit of the laser to smooth out the modulations and the spatial profile was shown to meet the specifications. The

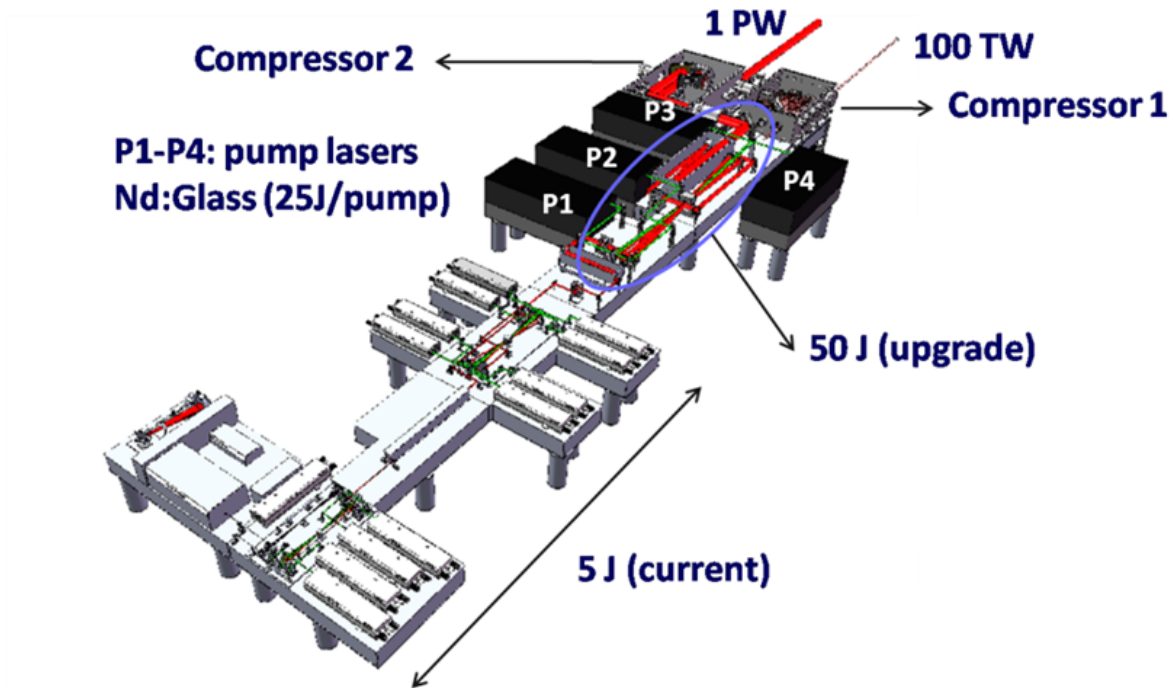


Figure 9: Layout of the high-power laser system at the University of Nebraska, Lincoln. The original 100 TW system has been upgraded to the PW peak power level, by the addition of a power amplifier, and pulse compressor. This stage is now operational and will be used for accelerating electrons and ions to GeV energy level.

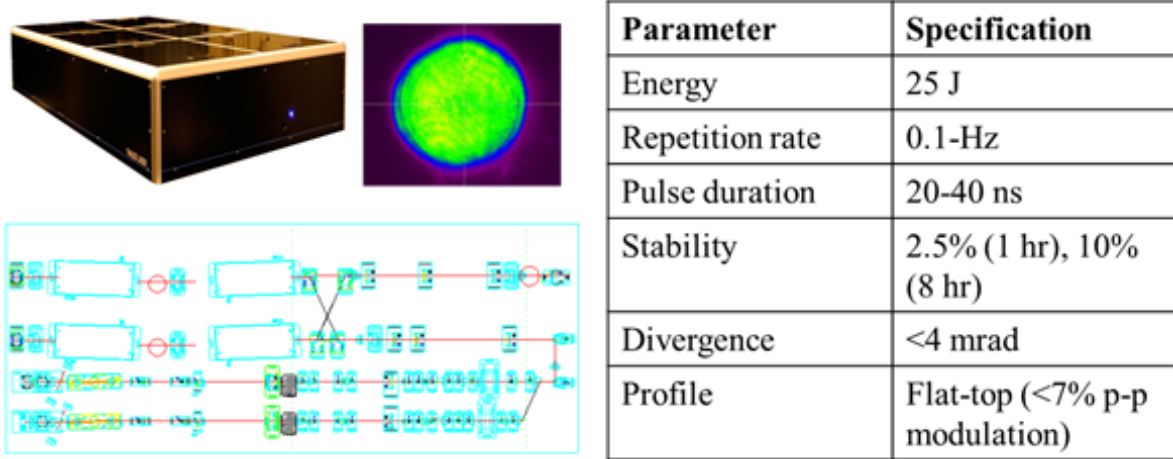


Figure 10: High-energy pump lasers for the PW amplifications system. The panel on the left shows the layout of each pump laser. It consists of two independent beamlets that are recombined into a single pulse at the output - a snapshot of the output beam profile is shown. The specifications for each of the four identical lasers are tabulated on the right.

pump lasers meet stringent stability criteria which is critical for applications of the laser system in high-intensity experimental research.

High-energy amplifier: The 5-J beam from the front end of the system is amplified in a large diameter Ti:S crystal pumped by the Atlas+ lasers. The efficiency of the amplification process is more for a smaller beam size. The choice of beam diameter is made based on the damage specifications of the optical components in the amplifier chain. The stretching factor of the system was increased from 300 ps to 500 ps to account for the final beam aperture in the compressor. The amplifier system is a standard bow-tie configuration consisting of 3-passes. The 10-Hz beam from the front end of the system is coupled into the amplifier through an independent beamline that expands the beam to the correct diameter using a telescope arrangement. The repetition rate is stepped down to 0.1-Hz by use of an optical shutter and the pump beams are temporally synchronized to the infrared beam by the use of a "MASTERCLOCK" that is driven by the clock of the laser oscillator and ensures synchronization with a precision of ~ 100 ps. A schematic of the amplifier assembly and specifications for the amplifier system is shown in Fig. 11. The infrared seed beam and the four pump beams are spatially overlapped on the crystal. At this time the beam size is 70 mm. This will be reduced to 65 mm to achieve maximum output. We have achieved 6-fold amplification in the final amplifier. The amplified energy matches the predicted

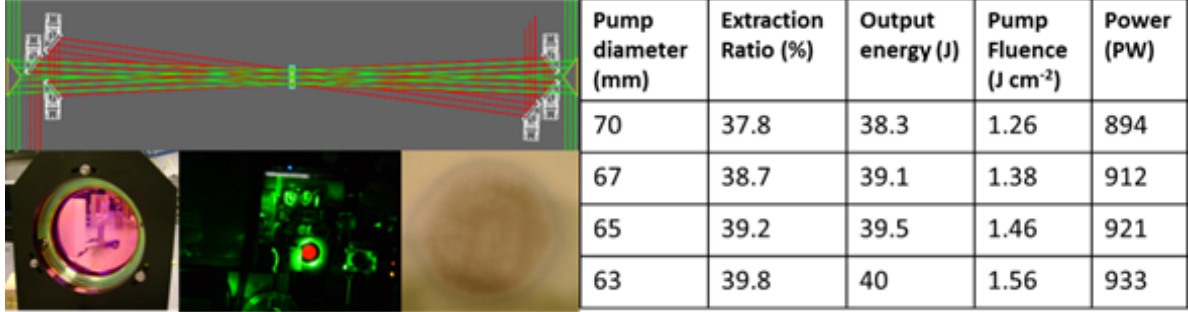


Figure 11: Amplifier system for the PW upgrade. The amplifier is a 3-pass bow-tie configuration. The 4 high-energy pump lasers are synchronized with the infrared beam from the front end and are incident on a large aperture (115 mm) Ti:S crystal. The left panel shows the layout of the amplifier, the large diameter Ti:S crystal used for amplification, the amplifier system in operation and a burn of the high-energy amplified beam. The specifications of the amplified infrared pulse are shown on the right.

gain based on calculations using the the Franz-Nodvik equations that model the operation of these amplifiers validating the design specifications for the amplifier.

Pulse compressor: The amplified beam with an energy of >40 J is expanded a final time to a diameter of 175 mm. This is needed to operate within the damage threshold of the compressor gratings. The compressor is a standard 2-grating, 4-pass configuration as shown in Fig. 6. The gold-coated compressor gratings (dimensions 60 cm \times 50 cm) were manufactured by LLNL. The amplified pulse with an energy > 40 J and diameter of 175 mm enters the compressor as shown. It is then reflected off the gratings four times and gets compressed to a pulse length of <30 fs. Each grating reflects $> 92\%$; hence the overall efficiency of the compressor is $\sim 70\%$. The compressor is equipped with motor drives (rotation and translation stages) to control the alignment at the micron level in both position and angle.

Diagnostics: The upgraded laser system is equipped with an array of diagnostics for complete spatial, spectral and temporal characterization of the beam. The spatial profile of the high-energy beam in the amplifier is measured by taking burns on sensitive paper or imaging the beam profile using an optical system coupled to a CCD. A large bandwidth, high-dynamic range optical spectrometer is used to measure the spectrum of the amplified pulse before and after compression. The laser is equipped with a spectral phase control system which is optimized to pre-compensate for gain narrowing in the power amplifiers and ensure the broadest spectrum at the output. This

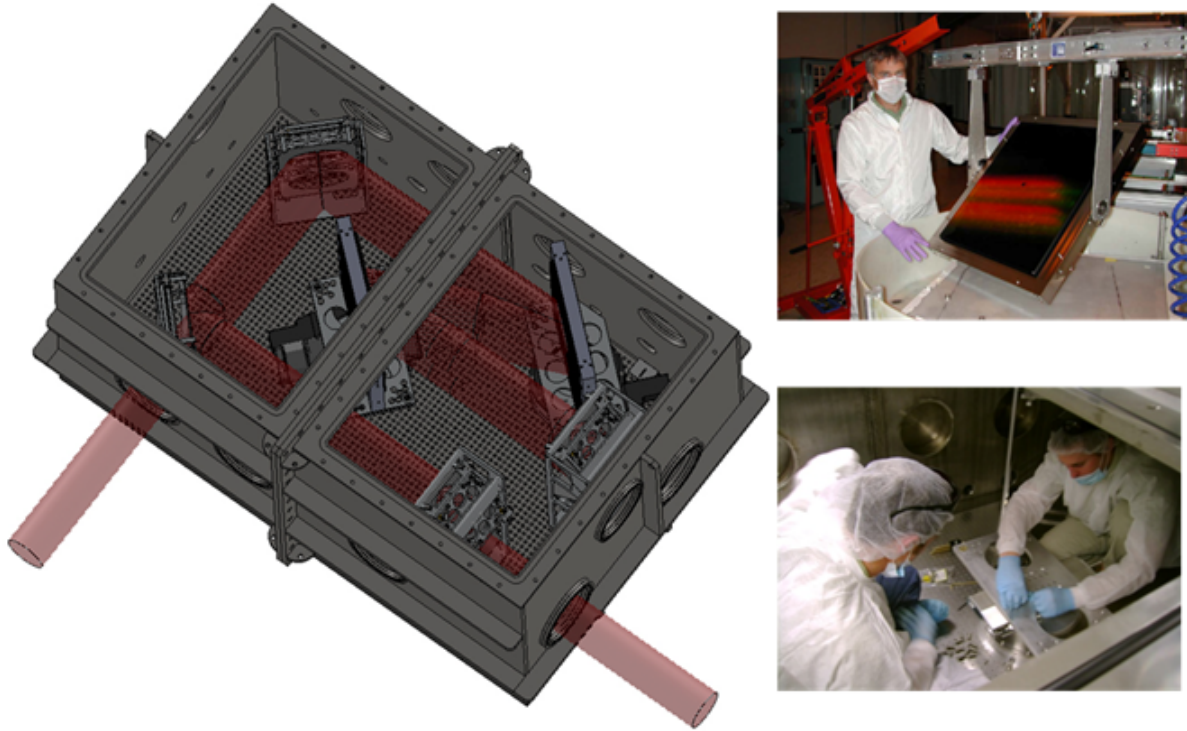


Figure 12: Pulse compression system for the PW stage. The layout of the 4-pass, 2-grating configuration is shown on the left. The compressor uses $60\text{cm} \times 50$ LLNL gold, gratings (top-right). The compressor chamber, and all optical mounts were manufactured in house. Assembly of the compressor is shown on the bottom-right panel.

condition ensures that the pulse can be compressed to < 30 fs. The energy of the beam is measured with standard, calibrated calorimeters. The pulse compressor output is optimized by using a second order autocorrelator to measure the temporal duration, an optical imaging system to correct for phase front tilt and a FROG device to measure and optimize the temporal phase of the beam.

E.5 PIC and fluid simulations of electron and ion acceleration

The acceleration of electrons to high energy has been modeled by use of fully explicit 3D PIC simulation. We use the quasi-cylindrical code CALDER-Circ [39], which preserves realistic geometry of interaction, and accounts for the axial asymmetry by decomposing electromagnetic fields (laser and wake) into a set of poloidal modes (whereas the particles remain in full 3D). Well preserved cylindrical symmetry during the interaction enables us to use just the two lowest order modes and thus reduce 3D problem to an essentially 2D one. We suppress the sampling noise by using large number of macroparticles (45 per cell) and high resolution in the direction of propagation, $dz = 0.125c/\omega_0$. The aspect ratio $dr/dz = 15.6$, and the time step $dt = 0.1244\omega_0^{-1}$. In addition, CALDER-Circ having fully self-consistent macroparticle dynamics, yields the complete electron phase space, and thus calculates precisely injected charge and beam emittance. The results of CALDER-circ simulations have been benchmarked against the the quasistatic, cylindrically symmetric, fully relativistic PIC code WAKE.

The generation of high-energy electron beams is modeled using both WAKE and CALDER-circ simulations with laser and plasma conditions corresponding to those measured in the experiment. Three-dimensional particle-in-cell (3D PIC) simulations using pre-ionized helium plasma with a trapezoidal profile (0.5 mm linear entrance, and exit ramps and a 2 mm plateau) and a Gaussian laser pulse with 42 TW power, central wavelength $0.805 \mu\text{m}$, duration 30 fs, and waist $13.6 \mu\text{m}$ have been performed. In all simulations, the plasma extends from $z = 0$ to 3 mm.

Nonlinear pulse evolution was studied using the quasi-static cylindrical code WAKE [38] with test particles [19]. We find that a position of the focal plane with respect to the plasma is critical for self-focusing, and hence the time of initiation, and termination of self-injection. Using the laser, and

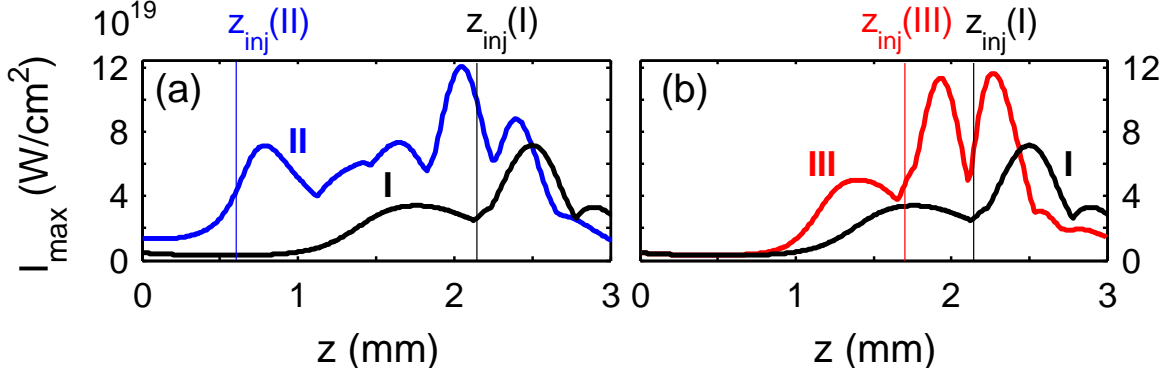


Figure 13: (a) Results of WAKE simulations showing evolution of the laser peak intensity for the parameters of Fig. 2(c) and different positions of the focal plane. Curve (I): focus before the plasma, $z_{\text{foc}} = -1$ mm; curve (II): focus at the plasma edge, $z_{\text{foc}} = 0$. (b) Effect of plasma density on the nonlinear pulse evolution for $z_{\text{foc}} = -1$ mm. Curve (I) corresponds to Fig. 2(c), and curve (III) to Fig. 2(b). Self-injection begins at positions $z_{\text{inj}}(\text{I} - \text{III})$.

plasma parameters of Fig. 2(c), we position the laser focus at two locations: (I) $z_{\text{foc}} = -1$ mm (the limit of experimental uncertainty), and (II) $z_{\text{foc}} = 0$. Fig. 13 shows the evolution of peak intensity. In case (I), the pulse entering the plasma has a large spot size $\approx 23 \mu\text{m}$, and a diverging wave front. It takes nearly 2 mm to refocus the pulse, create the bubble, and initiate self-injection. The slow evolution of the bubble suppresses continuous injection, leading to the formation of a monoenergetic bunch with minimal dark current. In case (II), the bubble forms near the plasma entrance; self-injection begins near the edge of the density plateau, and continues without interruption, resulting in a poorly collimated beam with a broad energy spectrum. Case (III) shown in Fig. 13(b) corresponds to the focal location of the case (I) but with the density corresponding to Fig. 2(b). At higher density, the pulse self-focuses sooner, and self-injection begins earlier, resulting in higher injected charge, and a broader energy spectrum.

Using the parameters for cases (I), and (III) of Fig. 13 we performed 3D PIC simulations using the quasi-cylindrical code CALDER-Circ [39, 20]. We suppressed sampling noise by using 45 particles per cell, and a longitudinal resolution of 50 grid points per λ_0 . To enable one-to-one comparison of the simulation with experimental data, electrons exiting the plasma were propagated through the experimental detection system using GPT. Simulated, and experimental spectra are shown in Fig. 7. Quasi-monoenergetic bunches shown in Figs. 14(a), and (b) are injected at the positions $z_{\text{inj}}(\text{I}) \approx 2.15$

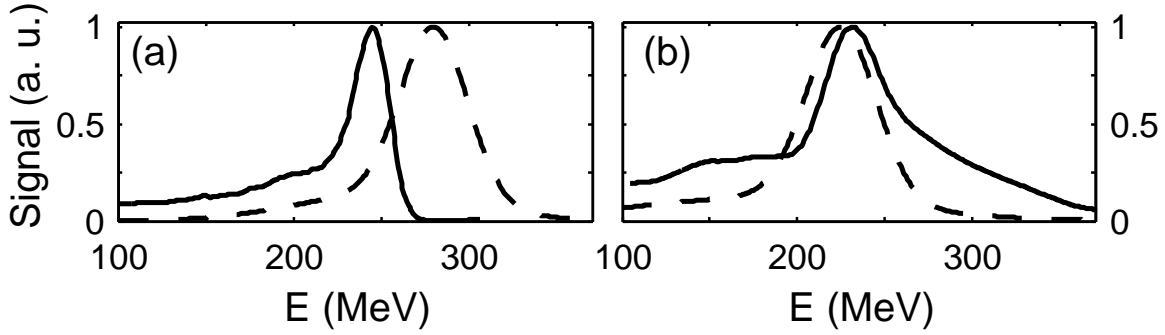


Figure 14: Lineouts of experimental (dashed), and simulated (solid) electron energy spectra corresponding to the parameters of Fig. 2(c) [panel (a)] and Fig. 2(b) [panel (b)].

mm, and $z_{\text{inj}}(\text{III}) \approx 1.7$ mm, respectively [as indicated in Fig. 13(b)]. Their energy, and charge are close to the experimentally measured values [entries (c), and (b) of Table 1]. At the same time, simulations overestimate the beam divergence roughly by a factor 3.5. Notably, using the optimal focal location drastically reduces dark current in the simulation of Fig. 14(a). In addition, electrons produced by continuous injection are poorly collimated, further reducing their signal on the detector plate. This explains the low level of dark current in the experiment. Independent simulations of these cases using VORPAL [40] in 3-D cartesian geometry reproduced the dynamics of injection, and parameters of the electron bunches with high precision. CALDER-Circ simulations with the same focusing geometry confirmed the absence of injection into the first bucket at densities below $5.5 \times 10^{18} \text{ cm}^{-3}$.

Detailed simulations not only provide a clear physical understanding of the mechanism that produced the electron beam but also, provide information on beam parameters that are difficult to measure directly. For the case of wakefield accelerated electron beams, it is expected that the beam size will be of the order of a few microns (close to the focal spot of the laser that was used to drive the wakefield) and a temporal duration of a few femtoseconds. This expectation is verified by a study of the spatio-temporal structure of the electron beam that is produced in the CALDER-Circ simulations. The results are shown in Fig. 15. The simulated electron beam spectrum agrees with the high-energy beams observed experimentally. The test particle coordinates and momenta are plotted to show the transverse source size and the temporal length. The computed source size is determined to be $< 10 \mu\text{m}$ with temporal duration < 10 fs. Thus the wakefield driven electron source

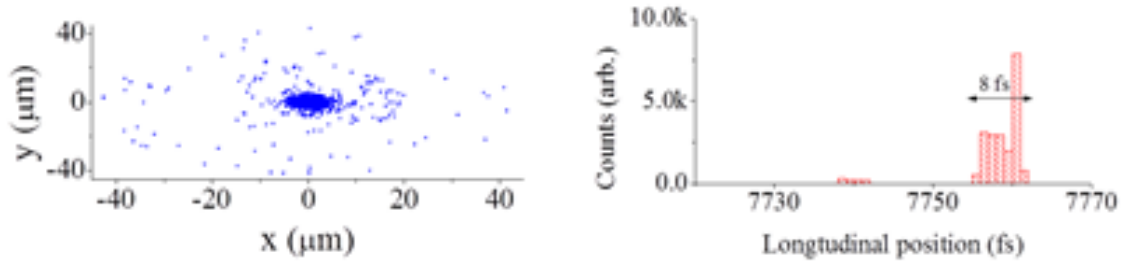


Figure 15: Spatio-temporal structure of the electron beam at the exit of the plasma. The conditions correspond to experiments with a 3 mm nozzle that produced > 300 MeV electron beams. The low energy component that is produced in the simulation has been filtered out and the results show that the high-energy electron beam has a source size and temporal duration significantly smaller than the corresponding parameters of the drive laser pulse.

produces beams with low transverse emittance and ultrashort duration.

E.6 Study limits of resolution and target thickness for imaging embedded cracks in DoD relevant samples with both electrons and ions beams

We have investigated the fundamental and practical limits of the use of laser-wakefield driven high energy electron beams for non-destructive radiographic imaging of sub-millimeter structures embedded within dense objects at stand-off distance. When an energetic electron beam travels through matter, the Coulomb force between the electrons and the nuclei in the medium leads to a loss of energy, along with a large number of small deflections in the electron trajectories. Electrons that penetrate dense material undergo significantly more elastic and inelastic collisions than those that traverse through air or low material density materials. As a result, the electrons lose energy as they propagate through matter, and their angular distribution becomes broader. The energy loss and angular spread depends on the total areal density traversed, and can be used to infer the characteristics of the medium through which the electrons propagated. The transmitted electrons can be efficiently detected on scintillator screens placed after the target material. A scintillating detector records the 2-D variations in deposited beam dose, with larger dose deficits corresponding to high areal density regions within the target material. The highly penetrating nature of high energy electron beams, coupled with their low divergence, enables efficient delivery to a distant target,

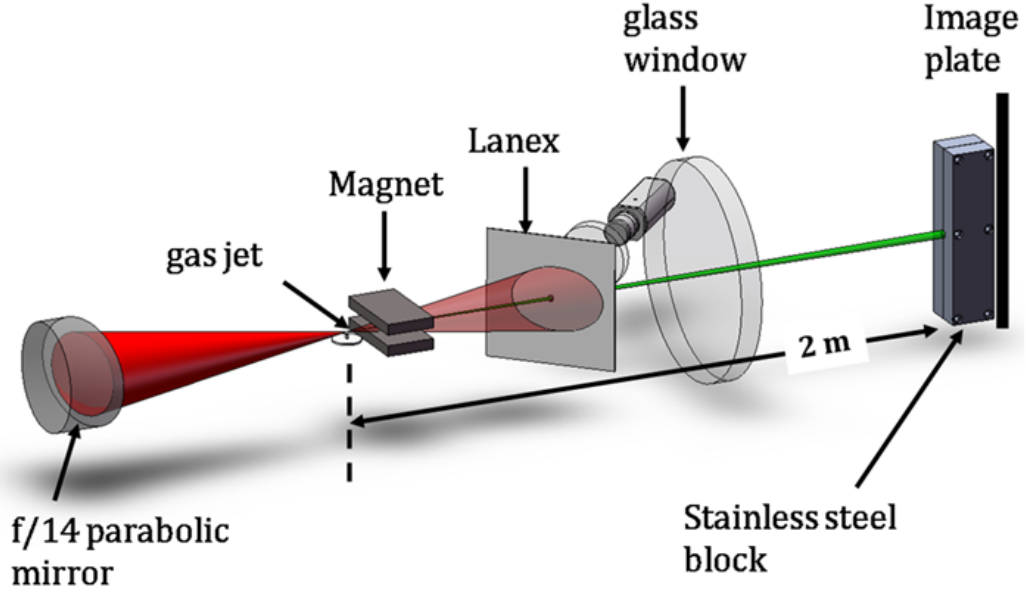


Figure 16: Experimental schematic for electron beam generation. An $f/14$ off-axis parabolic mirror focuses a laser beam to a waist of $15\ \mu\text{m}$ onto a supersonic gas nozzle. High-energy electron beams generated in the laser-driven from the resulting plasma are characterized using a magnetic spectrometer and they then impinge on a fluorescent screen (Kodak - LANEX), which is imaged using a 12-bit CCD camera. Also depicted in the schematic is the experimental setup to record radiographs of embedded structures of sub-millimeter resolution at standoff distance.

making them suitable for long standoff applications.

Prior work on radiography using electron beams from a laser wakefield accelerator were relatively low resolution ($\sim 1\ \text{mm}$), because the electron beam had a quasi-Maxwellian spectrum, predominantly containing low energy electrons. The highest resolution ($\sim 0.5\ \text{mm}$) radiographs previously obtained were recorded using bremsstrahlung generated x-rays, produced when a laser generated electron beam impinged on a Tantalum converter, with a source size inferred to be $320\ \mu\text{m}$. In this case, the object was placed in vacuum in close proximity ($\sim 10\ \text{cm}$) very close to the source and inside the same vacuum chamber as the source, which are conditions which are unsuitable for long standoff applications. We demonstrate direct electron beam radiographs that were performed with quasi-monochromatic high energy beams, for which small angle scattering is reduced. We were able to visually resolve embedded structures as small as $250\ \mu\text{m}$ wide and $2.54\ \text{cm}$ in length, with the object placed in air at a significant distance of several meters from the source. The

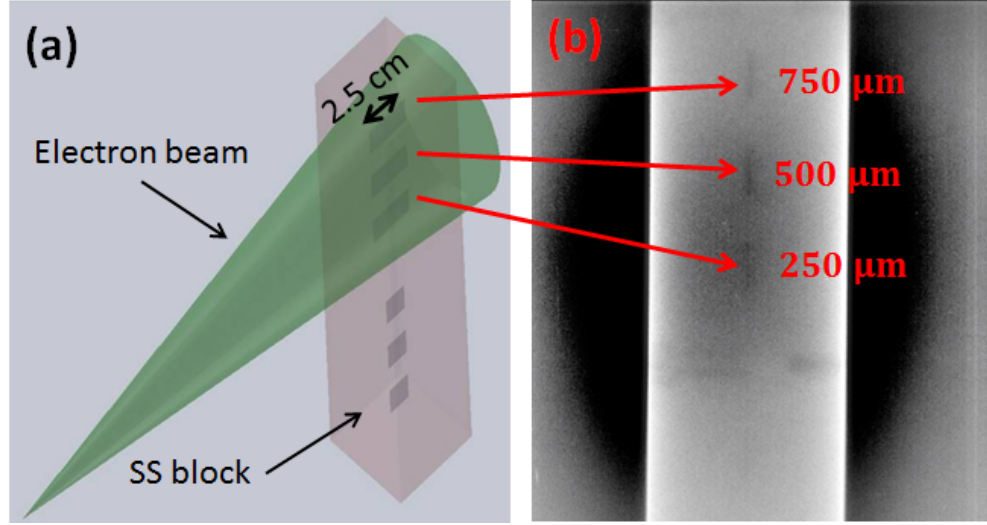


Figure 17: Three-dimensional representation of the stainless steel block with embedded voids. The electron beam used to image the voids is also shown schematically. (b) Experimental radiograph of the voids.

calculated resolution is $400\text{ }\mu\text{m}$. and limited by the signal to noise ratio.

The experimental setup used is shown in Fig. 16. The quasi-mono-energetic electron beams that are routinely obtained are tunable over an energy range of $50 - 400\text{ MeV}$, depending on the choice of acceleration distance (i.e., the nozzle diameter), plasma density, and laser intensity. For the purpose of radiography, 1.3 J of laser energy was focused over a 3 mm diameter gas jet, of the Laval type, with initial plasma density of $1 \times 10^{19}\text{ cm}^{-3}$. Radiographic images were obtained by interposing various objects between the electron beam source and a phosphor plate. For the results described below, the electron beam energy was $\sim 100\text{ MeV}$. On many of the shots, a lower energy beam at $\sim 30\text{ MeV}$ was also present. The electron beam is spatially and spectrally imaged on a fluorescent screen and propagates to the target after it exits the vacuum chamber through a glass window. The radiography objects consisted of 2.5 cm long voids were embedded within a 5 cm thick stainless steel block (shown in Fig. 17(a)), and placed 2 m from the supersonic jet. Three different side-by-side void thicknesses were imaged, with widths each of different width: of $250\text{-}\mu\text{m}$, $500\text{-}\mu\text{m}$, and $750\text{ }\mu\text{m}$. Ten electron beam shots, each with electron energy $150 \pm 20\text{ MeV}$ and an angular divergence of $4.7 \pm 0.5\text{ mrad}$, were used to acquire the radiograph shown in Fig. 17(b), which was recorded by an image plate placed behind the steel block.

The images of the void can be used to determine the resolving power of

the source. As a first step, in order to improve the signal-to-noise on these images, Fourier filtering techniques were used. This involves the use of a band-pass filter which eliminated features smaller than 3 pixels and larger than 40 pixels. The choice of the lower and upper cutoffs was based on the fact that the images of the voids being studied had a spatial size of 10 – 20 pixels. The result of applying this filter to the image in Fig. 17(b) is shown in Fig. 18(a). Fig. 18(b) shows a lineout of the 500 μm gap taken at location 2, as well as a Gaussian fit to the data. To compute the spatial resolution obtained by this method, the derivative of this lineout across the 750 μm gap was computed, and is shown in Fig. 17(c). The full width at half maximum (FWHM) of the derivative yields a resolution of 330 μm . To the best of our knowledge, this is the highest resolution ever achieved for a radiographic image of an embedded void.

Since the source size of the electron beam is expected to be $< 100 \mu\text{m}$, the measured source size, necessarily reflects the fact that the technique is limited by the size of the object being used. We computed the source size at different locations. As an example, a line-out taken at location 1, yields a source size of $\sim 410 \mu\text{m}$. Performing similar calculations at different locations on the void, yields an average source size of $400 \pm 100 \mu\text{m}$. Unfortunately, the low contrast of the 250 μm void prevented its use in computing the source size. This, to the best of our knowledge, is the first evidence of sub-millimeter electron beam radiograph at a distance of 2 m from the source.

In order to predict the performance of the electron beam radiography device and compare this with measurements, the different experimental scenarios were modeled by means of Monte-Carlo simulation code MCNPX v.2.5.0. Studies of the resolution possible with the laser-driven electron beam were numerically modeled assuming an electron beam emanating from a point source with a monochromatic energy of 150 MeV and a divergence of 4.7 mrad directed at the center of the 250 μm gap. Both electrons and photons were tracked in MCNPX using the default physics models and approximately 3×10^7 source histories. In order to expedite the calculation, electron tracking in the system ceases when the electron energy falls below 100 keV. These low energy electrons are produced as the source electrons slowdown in the target block. Geometric splitting was performed throughout the steel block to increase the electron population entering the image plate. The image-plate response was computed using an energy deposition mesh tally over its entire

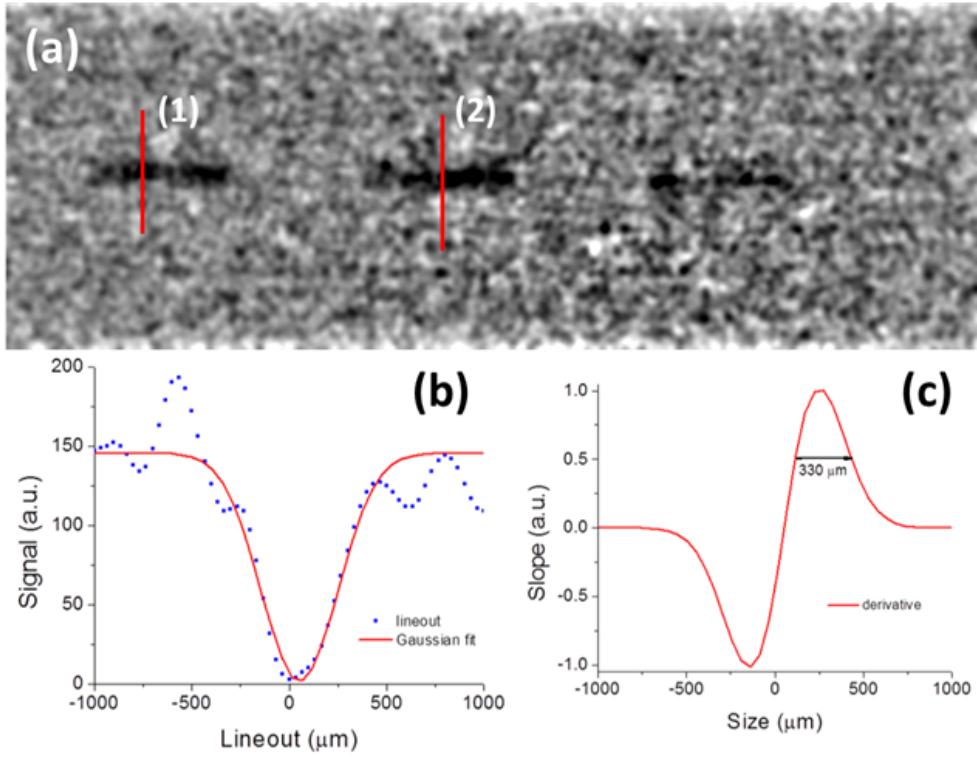


Figure 18: Electron radiographic images of voids embedded in steel (from left to right: 750 μm , 500 μm , and 250 μm). (a) Fourier enhanced image (red line indicates lineout location). (b) Lineout of crack (circles) and Gaussian fit (solid line). (c) Derivative of fitted profile indicates a source size of 330 μm

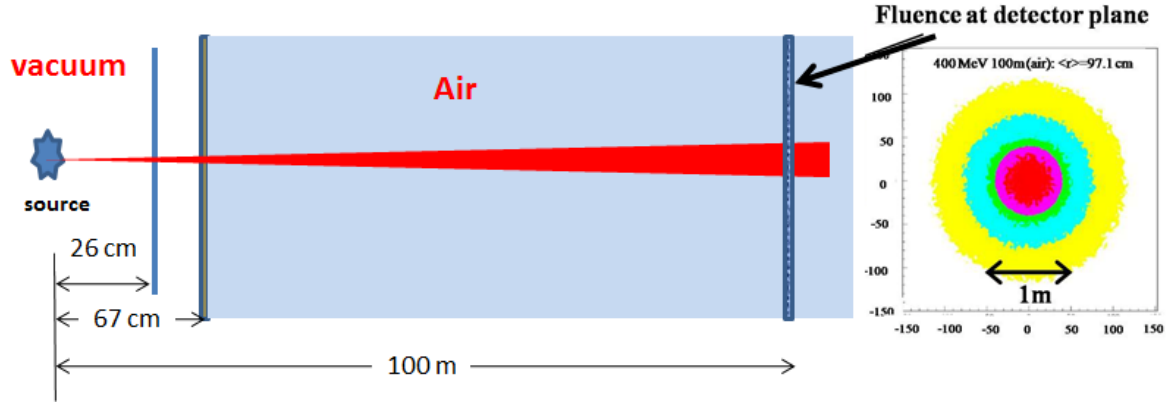


Figure 19: A Monte-Carlo simulation of a point source electron beam of energy 400 MeV with a cone angle of 8 mrad, exiting the vacuum chamber to reach a tally plane 100 m from the source. The electron beam spreads to a diameter of about a meter at this distance whereas the unscattered beam would measure 0.8 m in diameter, at the same distance from the source. The simulation work was performed by S. Pozzi *et al.*, University of Michigan, Ann Arbor.

plane. The total energy deposited from all the particles in each mesh cell by all the particles per unit volume is included. The mesh consisted of a 200×200 grid, averaged along the image plate thickness. These calculations are able to reproduce the features of the voids that are observed in experiments.

While it was impractical for us to experimentally conduct truly long stand-off studies (at distance of 10 – 100 m from the source), MCNPX simulations provided a reliable way to extend the results. A Monte Carlo model was developed to investigate the propagation of high-energy electron beams in air over significant distances. As an example of these calculations, we show in Figure 5 the propagation of a monoenergetic source of electron beam of energy 400 MeV. The choice of beam parameters is determined by experimentally measured characteristics. The beam travels a distance of 100 m from the source, in air to reach a tally plane. The computed electron fluence (normalized to maximum) of the resulting shower is also shown in Fig. 19. The electron beam spreads to a diameter of 1 m, $\sim 20\%$ higher than would be expected from geometrical considerations alone. The result indicates that a significant fraction of the electrons undergo little or no deflection through a distance of 100 m of air making it a good candidate for long standoff applications. Also, electron beams, unlike MeV photons, can be manipulated, redirected, or focused either before during and after interaction with the target.

F Progress towards program goals

The detailed description in the prior sections highlights the progress made during Phases I and II of the DARPA grant, and demonstrates that the proposed goals of the program were met. Significant improvements were made to the operation and control of the laser parameters in order to have a stable driver for optically driven sources of ionizing radiation. The development of a stable, high-brightness, laser wakefield accelerator fulfills the requirements set out for Module 1. Both self-injected and optically injected electron beams were produced and characterized in detail. Detectors for characterizing high-energy electron beams were developed and calibrated — the performance characteristics of the accelerator are now precisely known. Simulations using PIC and/or fluid models were performed to elucidate the mechanism underlying the generation of the high brightness electron beams, and this understanding permitted optimization of beam energy, energy spread, and charge. They also provide characteristics of the electron beam such as source size and divergence which are extremely challenging to measure in practice and demonstrate the the electron beams produced in laser wakefield accelerators have micron source sizes and femtosecond duration. Our 100 TW laser system has been upgraded to the PW peak power level by the addition of another amplification stage and a pulse compression system and will enable the development of a source of high-energy proton beams. The electron beams produced from Module 1 were used for radiography of embedded voids in steel blocks, demonstrating that our hyperspectral radiation source is viable for early detection of cracks in objects of relevance to DoD.

G Publications

G.1 Refereed journals

- S.Y. Kalmykov *et al.* “Electron self-injection into an evolving plasma bubble: Quasi-monoenergetic laser-plasma acceleration in the blowout regime,” *Phys. Plasmas* 18, 056704 (2011).
- V. Ramanathan *et al.* “Submillimeter-resolution radiography of shielded structures with laser-accelerated electron beams,” *Phys. Rev. Special Topics* 13, 104701 (2010).
- S. Banerjee *et al.*, “Quasi-monoenergetic, background-free, self-injected electron beams from a laser-plasma-bubble accelerator,” *Phys. Rev.* (submitted, 2010).

G.2 Conference proceedings

- S. Banerjee *et al.*, “Stable, Monoenergetic 50-400 MeV Electron Beams with a Matched Laser Wakefield Accelerator,” *Proceedings of the Particle Accelerator Conference*, 2009 (to be published in *Phys. Rev. ST-AB*).
- S. Banerjee *et al.*, “High-Brightness, Stable Electron Beams from a Laser Wakefield Accelerator Operating in the Matched Regime,” *The Conference on Lasers and Electro-Optics (CLEO)/The International Quantum Electronics Conference (IQEC)* (Optical Society of America, Washington, DC, 2009), JFB2.
- V. Ramanathan *et al.* “Laser-Plasma Generated Electron Beams for Radiographic Applications,” *The Conference on Lasers and Electro-Optics (CLEO)/The International Quantum Electronics Conference (IQEC)* , *OSA Technical Digest (CD)*, (Optical Society of America, Washington, DC, 2009), JFB6.
- S. Bagchi *et al.* “Measurement of Damage Threshold for Metallic Gratings under Intense Laser Pulse Irradiation,” *The Conference on Lasers and Electro-Optics (CLEO)/The International Quantum Electronics Conference (IQEC)*, , *OSA Technical Digest (CD)* (Optical Society of America, Washington, DC, 2009), JThE (2009).

Bibliography

- [1] K. Ertel *et al.*, RAL-TR-2006-025, 187, (2006).
- [2] K. Ertel *et al.*, RAL-TR-2007-025, 1717, (2007).
- [3] V. Chvykov and V. Yanovsky, CLEO Proceedings, OSA Technical Digest, Paper JWB4 (2009).
- [4] F. Druon *et al.*, Optics Letters **23**, 1043 (1998).
- [5] B. Kohler *et al.*, Optics Letters, **20**, 483 (1995).
- [6] S. P. D. Mangles *et al.*, Nature (London) **431**, 535 (2004).
- [7] C. G. D. Geddes *et al.*, Nature (London) **431**, 538 (2004).
- [8] J. Faure *et al.*, Nature (London) **431**, 541 (2004).
- [9] W. P. Leemans *et al.*, Nat. Phys. **2**, 696 (2006).
- [10] N. A. M. Hafz *et al.*, Nat. Photon. **2**, 571 (2008).
- [11] S. Kneip *et al.*, Phys. Rev. Lett. **103**, 035002 (2009).
- [12] D. Froula *et al.*, Phys. Rev. Lett. **103**, 215006 (2009).
- [13] C. E. Clayton *et al.*, Phys. Rev. Lett. **105**, 105003 (2010).
- [14] P. Dong *et al.*, Phys. Rev. Lett. **104** 134801 (2010).
- [15] M. H. Helle *et al.*, Phys. Rev. Lett. **105**, 105001 (2010).
- [16] J. B. Rosenzweig *et al.*, Phys. Rev. A **44**, R6189 (1991).
- [17] A. Pukhov and J. Meyer-ter-Vehn, Appl. Phys. B **74**, 355 (2002).
- [18] W. Lu *et al.*, Phys. Rev. ST Accel. Beams **10**, 061301 (2007).

- [19] S. Kalmykov *et al.*, Phys. Rev. Lett. **103** 135004 (2009).
- [20] S. Y. Kalmykov *et al.*, New J. Phys. **12**, 045019 (2010).
- [21] S. Y. Kalmykov *et al.*, Phys. Plasmas **18**(5) (2011) (in press).
- [22] S. Kneip *et al.*, Nat. Phys. **6**, 980 (2010).
- [23] F. V. Hartemann *et al.*, Phys. Rev. ST Accel. Beams **10**, 011301 (2007).
- [24] P. Sprangle, B. Hafizi, and J. R. Peñano, Phys. Rev. ST Accel. Beams **12**, 050702 (2009).
- [25] S. P. D. Mangles *et al.*, Phys. Plasmas **14**, 056702 (2007).
- [26] J. Osterhoff *et al.*, Phys. Rev. Lett. **101**, 085002 (2008).
- [27] A. Maksimchuk *et al.*, Appl. Phys. B **89**, 201 (2007).
- [28] R. C. Issac *et al.*, Proc. SPIE **7359**, 735915 (2009).
- [29] S. M. Wiggins *et al.*, Plasma Phys. Control. Fusion **52**, 124032 (2010).
- [30] D. Umstadter *et al.*, Phys. Rev. Lett. **76**, 2073 (1996).
- [31] V. Malka *et al.*, Phys. Plasmas **16**, 056703 (2009).
- [32] K. Schmid *et al.*, Phys. Rev. ST Accel. Beams **13**, 091301 (2010).
- [33] V. Ramanathan *et al.*, Phys. Rev. ST Accel. Beams **13**, 104701 (2010).
- [34] S. B. van der Geer *et al.*, in *Computational Accelerator Physics 2002* Vol. 175 (IOP, UK, 2005), p. 101.
- [35] S. P. D. Mangles *et al.*, Plasma Phys. Control. Fusion **48**, B83 (2006).
- [36] M. Tzoufras *et al.*, Phys. Plasmas **16**, 056705 (2009).
- [37] J. Faure *et al.*, Phys. Rev. Lett. **95**, 205003 (2005).
- [38] P. Mora and T. M. Antonsen, Jr., Phys. Plasmas **4**, 217 (1997).
- [39] A. F. Lifschitz *et al.*, J. Comput. Phys. **228**, 1803 (2009).
- [40] C. Nieter and J. R. Cary, J. Comput. Phys. **196**, 448 (2004).